

Isomer-to-isomer beta decay of $^{180}\text{Hf}^m$ and the nucleosynthesis of $^{180}\text{Ta}^m$

Stephen E. Kellogg*

Nuclear Physics Laboratory, University of Washington, Seattle, Washington 98195

Eric B. Norman†

*Nuclear Physics Laboratory, University of Washington, Seattle, Washington 98195
and Nuclear Science Division, Lawrence Berkeley Laboratory, Berkeley, California 94720*

(Received 27 May 1992)

The direct beta-decay branch linking $^{180}\text{Hf}^m$ ($t_{1/2}=5.5$ h) to $^{180}\text{Ta}^m$ has been measured to be $f_\beta=(0.29\pm 0.05\pm 0.06)\%$. The relevance of this decay for the nucleosynthesis of $^{180}\text{Ta}^m$ is discussed.

PACS number(s): 23.40.Hc, 27.70.+q, 95.30.Cq, 97.10.Cv

I. INTRODUCTION

The nuclide ^{180}Ta bears the distinction of being nature's rarest "stable" isotope. Furthermore, doubly-odd ^{180}Ta is the only nuclide not normally found in its ground state. Though the short-lived ground-state radioactivity of ^{180}Ta ($t_{1/2}^g=8.1$ h, $I^\pi=1^+$) was identified in the 1930's [1], the long-lived, high-spin isomer remained undiscovered until 1954 [2,3], while its spin (9^-) and placement (73 ± 2 keV above the 1^+ ground state) were uncertain until about 1979 [4-6]. An impressive lower limit has been established on the half-life of the isomeric state ($t_{1/2}^m > 1.2 \times 10^{15}$ yr) against the γ , β , and electron-capture decay channels open to it [7]. This stability is principally due to the collective behavior of the deformed rare-earth nuclei.

In addition to its unusual nuclear structure, ^{180}Ta presents itself as an astrophysical enigma. The principal nuclear-astrophysical production mechanisms, which seem so successful in explaining the abundances of the neighboring heavy nuclei, fail to account for the observed abundance of ^{180}Ta , in spite of its rarity (0.0124% of natural tantalum). It is evident from Fig. 1 that ^{180}Ta is bypassed by the slow (s) neutron-capture process which proceeds through the stable hafnium isotopes $^{176-180}\text{Hf}$. Furthermore, since ^{180}Ta is bracketed by the stable mass $A=180$ nuclei ^{180}Hf and ^{180}W , it is shielded from the β^- and β^+ decay paths following the rapid (r) neutron-capture process and the less-frequent p process which successfully describe the neutron-rich and neutron-poor nuclei, respectively. Any mechanism which *does* produce ^{180}Ta must successfully feed the high-spin isomer, since the ground-state population is quickly transmuted to ^{180}Hf and ^{180}W . Finally, the susceptibility of the isomer to *destruction* in environments which might equilibrate it with its short-lived ground state places constraints on a possible production site.

Two attempts have been made in recent years to account for the solar-system abundance of $^{180}\text{Ta}^m$ via a two-step branch off of the s and/or r neutron-capture process paths. Beer and Ward proposed that $^{180}\text{Ta}^m$ may be produced through a weak β -decay branch from $^{180}\text{Hf}^m$, which is known to be populated in the s process [8,9]. Yokoi and Takahashi have alternatively suggested an s -process production mechanism involving excited-state β decay of ^{179}Hf followed by neutron capture on $t_{1/2}=1.7$ yr ^{179}Ta [10]. This paper addresses the Beer and Ward theory, shown as a dashed double line in Fig. 1.

A. Astrophysical production of $^{180}\text{Ta}^m$

The salient features of the Beer and Ward theory are summarized in Fig. 2. An s -process contribution to the abundance of $^{180}\text{Ta}^m$ requires that (1) a fraction B of the thermal (stellar) neutron cross section on ^{179}Hf ($I^\pi=9/2^+$) produces the $I^\pi=8^-$ isomer of ^{180}Hf , and (2) a fraction f_β of the resulting $^{180}\text{Hf}^m$ population beta decays to the long-lived $I^\pi=9^-$ isomer in ^{180}Ta . If f_β proves to be too small for an exclusive s -process solution to the production of $^{180}\text{Ta}^m$, then the r process can make up the difference, providing (1) a fraction f_m of the β decays of ^{180}Lu [$I^\pi=(3^-, 5^+)$] leads to the population of the $I^\pi=8^-$ isomer in ^{180}Hf , followed by step (2) above. There are, in fact, two possible branch paths from $^{180}\text{Hf}^m$ to $^{180}\text{Ta}^m$: (a) the direct isomer-to-isomer, 214-keV-end-point β transition f_β , and (b) a weaker 113-keV-end-point β decay f'_β to an $I^\pi=8^+$ level in ^{180}Ta which readily decays by γ emission to the long-lived high-spin isomer. In an earlier study [12] we measured the strength of the weaker path to be $f'_\beta=0.023\%$, and presented an upper limit on the isomer-to-isomer path $f_\beta \leq 1.4\%$.

We can quantitatively write down the s - and r -process contributions to the observed solar-system abundance of $^{180}\text{Ta}^m$ in terms of these β -branch ratios. Following Beer and Ward [8], we express the s -process contribution by

$$\left[\frac{N_s}{N_\odot} (^{180}\text{Ta}^m) \right] = \frac{[\sigma^* N_s (A=180)]}{\sigma^* (^{180}\text{Ta}^m) N_\odot (^{180}\text{Ta}^m)} B f_\beta^s, \quad (1)$$

where $[\sigma^* N_s]$ is a slowly varying function of A obtained

*Present address: XonTech, Inc., 6862 Hayvenhurst Ave., Van Nuys, CA 91406.

†Present address: Nuclear Science Division, Lawrence Berkeley Laboratory, Berkeley, CA 94720.

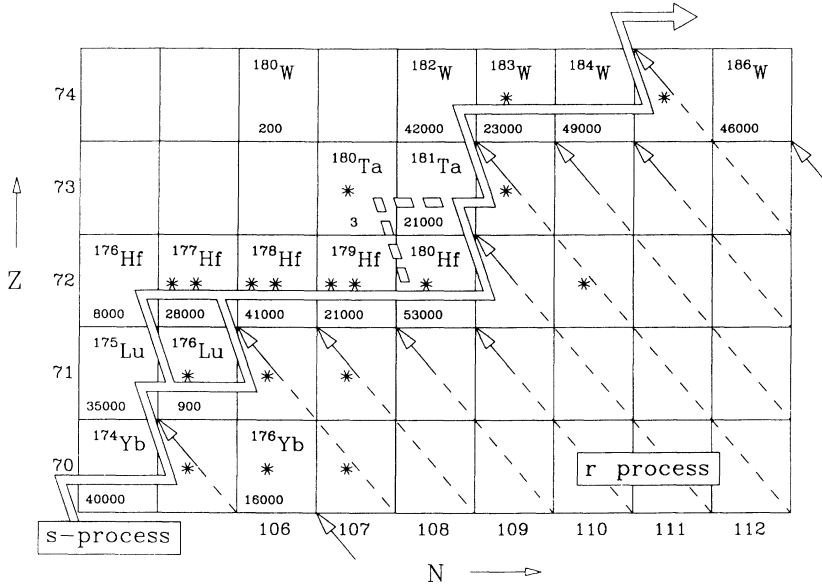


FIG. 1. Chart of the nuclides in the vicinity of ^{180}Ta . The stable nuclei are labeled and their solar-system abundances (relative to $[\text{Si}] = 10^{12}$) are given. The stars (*) denote K -isomeric states with half-lives greater than 1 s. The s -process path (double solid arrow) follows a well-defined path through the valley of beta stability. The decay routes from r -processed neutron-rich nuclei are shown by the dashed lines. Beer and Ward proposed that $^{180}\text{Ta}^m$ would be produced in the s and/or r process through the isomer-to-isomer beta decay of $^{180}\text{Hf}^m$ (double-dashed branch).

from a global fit to the neighboring “ s -process only” nuclei [13–15]. An analysis by Käppeler *et al.* gives $[\sigma^* N_s] = (5.53 \text{ mb} \times [\text{Si}] = 10^6)$ at $A = 180$ [16]. We assign an uncertainty of 5% to this systematically derived value.

The solar-system elemental abundances, N_{\odot} , are taken from the values of Anders and Ebihara [17] listed in Table I. The Ta abundance rests primarily on the analysis of a single C1 chondrite, but is supported by fractionation-corrected measurements in C2 chondrites and ratio-scaled measurements of Zr in C1 and C2 chondrites. Anders and Ebihara give an uncertainty in the Ta abundance of 10%.

In the absence of a direct measurement, the 30-keV neutron-capture cross section for $^{180}\text{Ta}^m$ was calculated by Beer and Macklin using a statistical model [9]. Their quoted uncertainty of 11% in the theoretical calculation mainly reflects uncertainties in the level density.

The branching ratio for a Boltzmann-weighted distribution of $kT = 30 \text{ keV}$ neutron energies is given by

$$B = \frac{\sigma^*(^{179}\text{Hf} \rightarrow ^{180}\text{Hf}^m)}{\sigma^*(^{179}\text{Hf})} \quad (2)$$

and is determined from the measured values in Table I to be $1.24 \pm 0.06\%$ [9]. This is not radically different from the branching ratio of 0.9% at thermal neutron energies.

Inserting these values into Eq. (1), we obtain

$$\left[\frac{N_s}{N_{\odot}}(^{180}\text{Ta}^m) \right] = (15.5 \pm 2.5) f_{\beta}^s, \quad (3)$$

where f_{β}^s represents the sum of all possible β -branch paths in a stellar environment from $^{180}\text{Hf}^m$ leading to the isomer of $^{180}\text{Ta}^m$. A pure 100% s -process production requires $f_{\beta}^s = 6.5 \pm 1.0\%$.

Two atomic effects due to the high degree of ionization in the stellar environment conspire to enhance the laboratory-measured values of the beta branches f_{β} [9]. First, the empty L shell blocks the internal conversion of

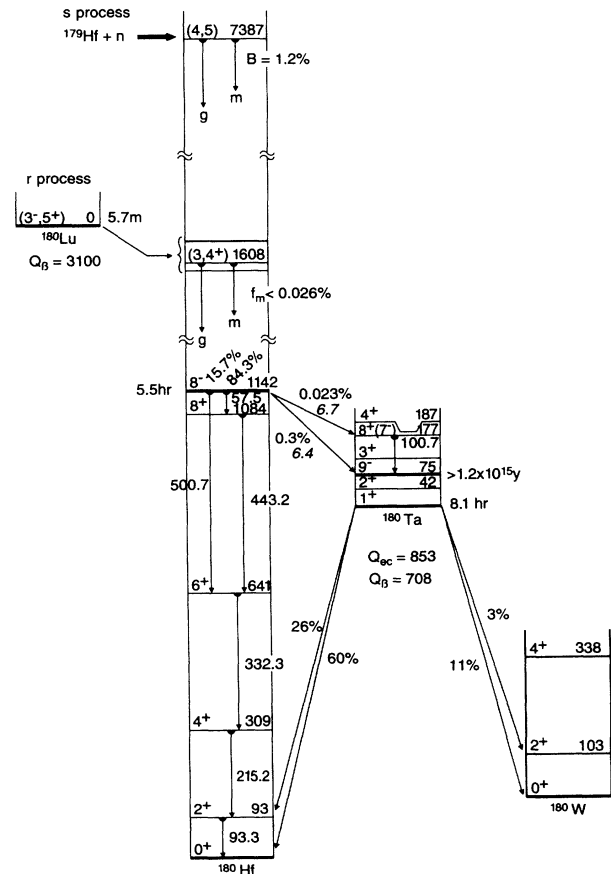


FIG. 2. Production (nuclear-astrophysical) and decay (laboratory) schemes of $^{180}\text{Hf}^m$. Allowed Gamow-Teller beta transitions from the isomer compete with K -inhibited gamma transitions to the ground-state rotor. We here describe a measurements of f_{β} , the direct isomer-to-isomer beta decay that populates $^{180}\text{Ta}^m$. This key branch is a gateway to the Beer and Ward model for the production of $^{180}\text{Ta}^m$ in the s and/or r process. Level placements and branching ratios are taken from Ref. [11].

TABLE I. Solar-system abundances and neutron cross sections needed to determine ^{180}Ta production in neutron-capture processes. Elemental abundances normalized to $[\text{Si}] = 10^6$ are taken from the reviews of Cameron [19] and Anders and Ebihara [17]. Isotopic fractions are taken from Lederer and Shirley. The cross sections are for a $kT = 30$ keV Boltzmann distribution of neutron energies and are mostly taken from the recent review of Bao and Käppeler [18]. A calculated cross section for unstable ^{179}Ta is included.

Elemental abundance	Ref. [19]	Ref. [17]	Isotopic fraction	σ^* (mb) (Ref. [1])	σ references
Hf	0.17	0.176(12)	^{178}Hf 27.1%	310(10)	[18,9]
			^{179}Hf 13.7%	991(30)	[18,9]
			$^{179}\text{Hf}(n, \gamma)^{180}\text{Hf}^m$	13.5(6) ^a	[8]
			^{180}Hf 35.2%	175(5)	[18,9]
Ta	0.020	0.0226(23)	$^{179}\text{Ta}(t_{1/2} = 1.7 \text{ y})$	3250 ^b	[10,20]
			^{180}Ta 0.0123%	1800(200) ^b	[18,9]
				2273 ^b	[20]
				3270 ^b	[21]
		^{181}Ta 99.9877%	733(37)	[18,22]	
W	0.15	0.137(10)	^{180}W 0.13%	669 ^b	[18,21]
				500 ^b	[10]
			^{182}W 26.3%	274(8)	[18,23]

^aPartial cross section for the production of $^{180}\text{Hf}^m$.

^bCalculated.

the 57-keV transition, increasing the $^{180}\text{Hf}^m$ partial half-life against γ decay by a factor of 1.4. Second, the nearly empty K shell allows the possibility of bound-state beta decay which significantly supplements the β -decay strength into the continuum. We can then express the β -decay enhancement-factor as

$$F_s^{\text{enh}} = \left[\frac{1}{\sum_j I_\gamma(j) \left\{ 1 + \sum_k \alpha_k(j) [n_k / 2(2k+1)] \right\}} \right] \times \left[1 + \frac{\lambda_{\beta B}}{\lambda_{\beta C}} \right], \quad (4)$$

where $I_\gamma(j)$ is the absolute gamma intensity for the j th isomeric (electromagnetic) transition, α_k is the internal conversion coefficient, and n_k is the mean electron number occupancy for the k th shell. Using the Strömberg formula [24] we calculated $0 \lesssim n_k \ll 2(2k+1)$ for the L and higher shells over the range of s -process pressures and temperatures. Beer and Macklin used the formalism of Bahcall [25] to estimate a bound-state-to-continuum β -decay ratio $\lambda_{\beta B} / \lambda_{\beta C} = 0.5$. Results of a recent calculation by Takahashi [26] using the formalism developed by Takahashi and Yokoi [27] show that $\lambda_{\beta B} / \lambda_{\beta C}$ for the 214-keV-end-point direct isomer-to-isomer decay varies from 0.5 to 3.0 for the range of temperatures and densities considered. A similar calculation for a 110-keV-end-point β transition, yields $\lambda_{\beta B} / \lambda_{\beta C}$ values between 1.5 and 11.0. Plausible s -process conditions cover the range of kT from 15 to 35 keV and densities from 100 to 10^4 g cm^{-3} [28]. Using nominal values of $kT = 25$ keV and $\rho = 1000 \text{ g cm}^{-3}$ of He matter, we

obtain $F_s^{\text{enh}}(214) = 1.4 \times (1 + 2.5) = 4.9$ and $F_s^{\text{enh}}(113) = 1.4 \times (1 + 9.0) = 14$ for the 214- and 113-keV-end-point β branches, respectively. We can then write $f_\beta^s = 4.9f_\beta + 14f'_\beta$, which can be inserted in Eq. (3) to obtain

$$\left[\frac{N_s}{N_\odot} (^{180}\text{Ta}^m) \right] = 76f_\beta + 220f'_\beta. \quad (5)$$

Our previously measured value of $f'_\beta = 0.023\%$ [12] can only contribute approximately 5% to the observed abundance of ^{180}Ta . A laboratory value of $f_\beta \approx 1.3\%$ for the direct transition is needed to account for the balance of nature's $^{180}\text{Ta}^m$ via the s process.

To extract the r -process contribution to the solar-system abundance of $^{180}\text{Ta}^m$, it is necessary to determine the fraction of ^{180}Hf produced in the r process. Using values from Table I, Beer and Macklin subtracted the s -process component to show that 51% of ^{180}Hf is populated by the r process. We can numerically express the r -process contribution to $^{180}\text{Ta}^m$ as a product of the two β branches:

$$\left[\frac{N_r}{N_\odot} (^{180}\text{Ta}^m) \right] = (1.2 \pm 0.2) \times 10^4 f_m f'_\beta \quad (6)$$

where here f'_β is the $^{180}\text{Hf}^m$ branch under stellar conditions valid for a *post-r* process. The stellar conditions for the s and *post r* processes may be quite different. Since the actual r -process site is unknown, we do not *a priori* know what enhancement factors due to ionization we should include. It is believed that the r process involves a transient high-temperature spike of short duration (≤ 100 s). If, for example, the r process takes place dur-

ing the cataclysmic ejection of material by a supernova, it is reasonable to suppose that the temperature and density will be greatly diminished hours later when the $^{180}\text{Hf}^m$ decay of interest occurs. Therefore, we use the laboratory value in our calculation: $f'_\beta = 1.0f_\beta + 1.0f'_\beta \approx f_\beta$. We have previously established a limit on the ^{180}Lu branch of $f_m \leq 0.026\%$ [29], which severely restricts any r -process component. A 50% r -process contribution to the solar-system abundance of ^{180}Ta would require $f_\beta \geq 18\%$, which is disallowed by Gallagher's previous limit [30]. We note, however, that our measured value of f_m differs markedly from that of Eschner *et al.* who found $f_m = 0.46 \pm 0.15\%$ [31]. Attempts to reconcile this difference by searching for a possible high-spin isomer of ^{180}Lu have been fruitless to date [32,33].

B. Nuclear structure of the isomers

The so-called "rare-earth" nuclei ($150 < A < 190$), to which ^{180}Ta belongs, lie far from any shell closures and have large prolate deformations. Rotational bandhead states are characterized by the Nilsson orbital quantum numbers $K^\pi[Nn_3\Lambda]$, where K is the projection of the total angular momentum on the body-symmetry (z) axis [34,35]. The $I^\pi = K^\pi = 9^-$ isomer in odd-odd ^{180}Ta is formed by a spin-aligned coupling of the proton and neutron quasiparticles $\frac{9}{2}^- [514]_\pi$ and $\frac{9}{2}^+ [624]_\nu$. The 8^- isomer in even-even ^{180}Hf can be formed either by breaking a proton pair and coupling the proton quasiparticles $\frac{7}{2}^+ [404]_\pi$ and $\frac{9}{2}^- [514]_\pi$ or by breaking a neutron pair and coupling $\frac{9}{2}^+ [624]_\nu$ and $\frac{7}{2}^- [514]_\nu$. There are two observed 8^- levels in ^{178}Hf , at 1147.4 keV (a 4.0 s isomer) and at 1479.0 keV, which have been shown to be substantial mixtures of just these two states [36–38]. By the time two more neutron orbitals have been filled in ^{182}Hf , the low-lying 8^- level (a 61.5 min isomer) is nearly a pure broken proton-pair configuration [39,40]. The calculated magnetic moments for the two configurations are quite different: $\mu(8^-)_{2\pi} = +8.2\mu_N$ and $\mu(8^-)_{2\nu} \leq 0.2\mu_N$. On the basis of its large measured magnetic moment of $\mu = (8.6 \pm 1.0)\mu_N$ [41,42], the isomer in ^{180}Hf ought to be primarily a broken-proton pair (2π) configuration as in $^{182}\text{Hf}^m$. However, the magnetic moment is not sensitive to a small ($\leq 10\%$) admixture of the broken-neutron pair (2ν) state. Further, the neutron transfer reaction $^{179}\text{Hf}(d,p)$ successfully produces the isomer suggesting that the admixture must be significant [43]. The higher-lying, predominantly two-neutron 8^- level has yet to be identified.

The β^- decay of the Hf $8^-_{(2\pi)}$ component to the 9^- isomer involves the hindered transition $\frac{9}{2}^+ [624]_\nu \rightarrow \frac{7}{2}^+ [404]_\pi$ which is seen in the β^- decay of ^{177}Yb and in the electron capture of ^{181}W with $\log ft$ values of 6.5 and 6.7, respectively. A $\log ft$ of 6.4 is observed in the analogous β^- decay of $^{182}\text{Hf}^m$. The β^- decay of the Hf $8^-_{(2\nu)}$ component to $^{180}\text{Ta}^m$, on the other hand, involves the unhindered transition $\frac{7}{2}^- [514]_\nu \rightarrow \frac{9}{2}^- [514]_\pi$. Fast $\log ft$ values of 4.7 and 4.4 are seen in the decays of the odd mass nuclei ^{175}Yb and ^{181}Os . Neighboring $^{182}\text{Hf}^m$ is observed to decay to the 7^- level in ^{182}Ta at 1162 keV via this mode with a $\log ft$

value of 4.8. A 10% admixture of the two-neutron configuration in $^{180}\text{Hf}^m$ ought to increase the β^- -decay strength to $^{180}\text{Ta}^m$ by a factor of 10. In his experimental search for f_β , Gallagher was motivated to measure this mixing. The limit $f_\beta \leq 3.8\%$ ($\log ft \geq 5.4$) established by Gallagher in 1962 is consistent with a 10% broken-neutron pair admixture [30].

II. EXPERIMENT

To measure the direct isomer-to-isomer transition, we are left with no alternative but to detect the low-energy β rays. We are confronted by two formidable backgrounds: (1) internal conversion electrons from the decay of $^{180}\text{Hf}^m$, and (2) contamination with the 408-keV-end-point β spectrum from the decay of ^{181}Hf .

A. Design

The dominant electromagnetic decay mode of the $t_{1/2} = 5.5$ h ^{180}Hf isomer yields an average of 3.0 γ rays and 1.5 internal conversion electrons as the nucleus "spins down" through the ground-state rotational band (Fig. 2 and Table II). The electron spectrum of $^{180}\text{Hf}^m$ is often characterized as a "picket fence" because of the nearly equal energy spacing between 9 strong lines ranging up to 500 keV. The lowest energy conversion lines from the 57-, 93-, and 215-keV transitions are the strongest and span the range of energy in which we can look for a 214-keV-end-point β spectrum. The valley between the $LM93$ and $K215$ peaks necessarily contains scattered events from the $K215$ and all higher energy conversion lines. In our experiment to measure f_β , the high resolution afforded by a magnetic spectrometer was sacrificed for the opportunity to veto conversion electron events. This is possible because of the inherently high γ multiplicity in the cascade decay of $^{180}\text{Hf}^m$. Each conversion electron has an associated x ray and on average 3γ rays in coincidence with it. An electron from the β decay of $^{180}\text{Hf}^m$ directly to $^{180}\text{Ta}^m$, on the other hand, travels unaccompanied by any other detectable radiation.

Our experimental setup is shown in Fig 3. A thin $^{180}\text{Hf}^m$ source was mounted about 1 cm from the front face of a solid-state detector thick enough to stop 400-

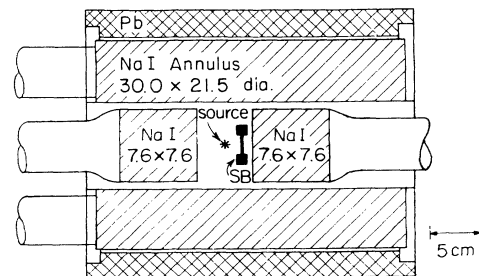


FIG. 3. Experimental setup. The $^{180}\text{Hf}^m$ source was mounted in close geometry to a surface barrier (electron) detector. These were surrounded by a 4π array of NaI (gamma) detectors to veto electron-gamma coincident events.

TABLE II. Absolute gamma and conversion-electron line intensities for $^{180}\text{Hf}^m$. The intensities (1000=100%) are mostly taken from the work of Christams and Cross [44]. Since conversion electrons from the L , M and higher shells are unresolved in this experiment, we show summed intensities and weighted energies for the “ LM ” lines. Measured and theoretical rejection factors F_{rej} defined in Eq. (7) for some of the electron lines are given. The theoretical factors are obtained using the approximate γ -detection efficiencies listed in the upper-right column.

γ line	E_γ (keV)	I_γ	I_{eK}	I_{eLM}	ϵ_{NaI} (%)
Hf K x	55.	363			50
$\gamma 57$	57.53	535		308	50
$\gamma 93$	93.33	175	190	635	61
$\gamma 215$	215.24	815	111	74	89
$\gamma 332$	332.28	944	40	16	91
$\gamma 443$	443.16	921	16.5	5.3	89
$\gamma 501$	500.69	148	5.6	3.1	89
Total events/Decay		3.801	0.363	1.041	
IC_e line	E_e (keV)	I_e	$F_{\text{rej}}^{\text{meas}}$	$F_{\text{rej}}^{\text{theor}}$	
$K 93$	28.0	190		447	
$LM 57$	48.6	308		948	
$LM 93$	85.1	635	464 ± 60	474	
$K 215$	149.9	111	325 ± 100	250	
$LM 215$	206.8	74	210 ± 60	124	
$K 332$	266.9	40	220 ± 100	141	
$LM 332$	323.6	16		70	
$K 443$	377.8	16.5		163	
$LM 443$	434.4	5.3		81	
$K 501$	435.3	5.6		107	
$LM 501$	492.8	3.1		53	

keV electrons. The source-detector assembly was mounted inside a 4π array of NaI scintillators to catch the γ rays in coincidence with the conversion electrons. The solid-state electron detector consisted of a “transmission-type” Si surface barrier detector with an active area of 300 mm^2 and a depletion depth of $712 \mu\text{m}$. The front surface electrode was a $40.1 \mu\text{g cm}^{-2}$ thick Au layer and the back surface electrode was the same thickness of Al. The 4π NaI scintillator array consisted of an annular detector 30.0 cm long $\times 21.5 \text{ cm}$ outer diameter with an 8.9 cm inner diameter, and two $7.6 \text{ cm} \times 7.6 \text{ cm}$ crystals which closed the ends of the annulus. The annulus has an inner wall Al thickness of 0.81 mm while the $7.6 \times 7.6 \text{ NaI}$ crystals were enclosed in 0.51-mm-thick chrome-plated Al cans. Since we wanted our NaI array to have a threshold below the 55-keV Hf K x rays, we found it necessary to operate the annular crystal’s six phototubes in the dark noise. A valid annulus signal was taken to be a coincidence between the summed output of tubes 1, 3, and 5 and the summed output of tubes 2, 4, and 6.

Surface barrier events were routed according to whether there was a coincident NaI event (VETO route) or not (NO VETO route). Electronic noise and electron straggling established an effective low-energy threshold of 35 keV . Above this threshold there were two “valleys” in which we could look for the β spectrum: (1) between the $LM 57$ and $LM 93$ peaks at about 55 keV , and (2) between the $LM 93$ and $K 215$ peaks at about 110 keV . We shall henceforth refer to these energy regions as the

$LM 57\text{-}LM 93$ and $LM 93\text{-}K 215$ valleys, respectively.

The $t_{1/2} = 5.5 \text{ h}$ $^{180}\text{Hf}^m$ source is most readily made in the $^{179}\text{Hf}(n, \gamma)$ reaction with a thermal neutron source. The neutron cross section for production of the isomer is 0.4 b . Any isotopically enriched ^{179}Hf source also contains residual quantities of the other hafnium isotopes and (n, γ) production of several other hafnium radioactivities is possible. Of particular concern to our study is the $t_{1/2} = 42.4 \text{ d}$ ^{181}Hf activity which is produced in the $^{180}\text{Hf}(n, \gamma)$ reaction with a thermal neutron cross section of 14 b . As is apparent in Fig. 4 and Table III, ^{181}Hf decays by β emission to two excited states in ^{181}Ta which subsequently cascade to the ground state by γ emission with a multiplicity of about 2. The electron continuum spectrum has β end-point energies of 405 and 408 keV , about twice as large as the end-point energy of the expected $^{180}\text{Hf}^m$ β -decay branch. The 133-keV transition is highly converted and the energy of the strong $K 133$ and $LM 133$ internal conversion lines unfortunately happen to fall in the two “valleys” ($LM 57\text{-}LM 93$ and $LM 93\text{-}K 215$) in which it is possible to look for the 214-keV β spectrum. The ^{181}Hf conversion lines and continuous β spectra form a major source of background, complicating our search for f_β .

The general method of dealing with the ^{181}Hf background is to accumulate spectra over a several day period and subtract the longer-lived ^{181}Hf component. The subtraction proves to be substantial and a primary source of statistical and systematic error. To extend our veto technique to include the beta continuum from the ^{181}Hf de-

TABLE III. Absolute gamma and conversion-electron line intensities for ^{181}Hf . Intensities (1000=100%) from Ref. [1] have been adjusted to guarantee proper line summing. The unresolved 133-, 136-, and 137-keV conversion transitions are combined in the lower table. Computations of F_{rej} explicitly include the β groups and the $t_{1/2} = 17.8 \mu\text{s}$ metastable state in ^{181}Ta .

γ line	E_γ (keV)	I_γ	I_{eK}	I_{eLM}	ϵ_{NaI} (%)
<i>Ta KX</i>	57.	328			50
γ 133	133.0	408	204	318	75
γ 136	136.2	55	66	22	75
γ 137	136.9	28	28	11.1	75
γ 346	345.8	135	5.4	2.2	92
γ 476	476.0	15	2.4	0.6	89
γ 482	482.0	810	22	4.0	89
γ 615	615.5	2.5	0.5	0.1	84
Total events/Decay		1.781	0.328	0.358	

IC_e line	E_e (keV)	I_e	$F_{\text{rej}}^{\text{meas}}$	$F_{\text{rej}}^{\text{theor}}$
<i>K</i> 133 } <i>K</i> 136 } <i>K</i> 137 }	69.0	298	19.2±2.9	16.6
<i>LM</i> 133 } <i>LM</i> 136 } <i>LM</i> 137 }	124.8	351	9.5±0.6	7.94
<i>K</i> 346	280.5	5		5.89
<i>LM</i> 346	337.8	2		2.79
<i>K</i> 482	416.7	24	5.3±0.9	2.35
<i>LM</i> 482	772.2	4.6	1.7±0.4	0.84
<i>K</i> 615	548.1	0.5		0.82
<i>LM</i> 615	607.5	0.1		0.00
β 408		920	7.66±0.26	7.13

decay, we note that 93% of the β strength directly feeds the $I^\pi = \frac{1}{2}^+$ level in ^{181}Ta at 615.2 keV or excitation. This level has a half-life of 17.8 μs . The two subsequent γ -ray transitions are in delayed coincidence with the beta rays. To render the beta rays eligible for vetoing, we intro-

duced a digital time delay within the microprogrammable branch driver (MBD) in the on-line data acquisition interface.

B. Procedure

A 0.65 mg sample of HfO_2 isotopically enriched to 89% ^{179}Hf with 8% ^{180}Hf content was bombarded at the University of Washington reactor ($\phi = 1.2 \times 10^{12}$ neutrons $\text{cm}^{-2} \text{s}^{-1}$) for 2 h to produce about 6 μCi of $^{180}\text{Hf}^m$. The activated sample was counted 2 h later with a Ge(Li) detector at the University of Washington Nuclear Physics Laboratory to verify that there were no short-lived contaminants. A thin source was prepared by first dissolving the fine granules of the oxide in 1 ml of hot, concentrated HF acid, and then drying a few 100 μl of this solution on a 50 $\mu\text{g cm}^{-2}$ carbon foil premounted on a 1-mm-thick plastic backing. The HfF_4 salt residue stuck to the carbon foil and was left uncoated. From the spot size and measured activity we calculated a source thickness of 20 $\mu\text{g cm}^{-2}$.

The Si detector was mounted on the front face of one of the 7.6×7.6 NaI. There was enough clearance between the 7.6×7.6 NaI and annulus inner wall to route a microdot cable to the enclosed Si detector, as well as a flexible hose to purge the enclosure with dry nitrogen. The N_2 purging procedure was necessary to retard the contamination of the surface barrier detector with HF vapor emanating from the source. With the N_2 purge operating, the source was mated to the detector in a fixed

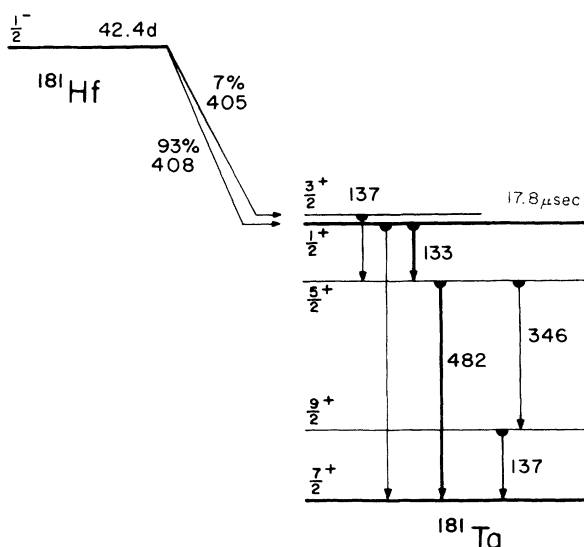


FIG. 4. The decay scheme of ^{181}Hf . The gamma cascade is in delayed coincidence with most beta rays because of the metastable ($t_{1/2} = 17.8 \mu\text{s}$) level at 615.2 keV of excitation in ^{181}Ta .

and reproducible position about 1 cm from the surface barrier face. Finally, the source-detector assembly was installed in the annulus and counting was begun.

Pulses from the surface barrier detector were amplified and fed into an analog-to-digital converter (ADC) and into a single-channel analyzer (SCA). The SCA was used to start a time-to-pulse-height converter (TAC). The TRUE START output from the TAC (verifying that the TAC had a valid start) was used as the logical GATE to the surface barrier ADC. If the logical GATE was received, the surface barrier signal was promptly converted, but then latched onto by the MBD for approximately $100\ \mu\text{s}$ while the MBD watched for the conversion of the TAC ADC. An SCA on the logically OR-ed signal from the NaI array was used to stop the TAC. The TAC was strobed a fixed $75\ \mu\text{s}$ after each start. If a TAC STOP signal was received during this time, the TAC ADC converted and the digitized Surface Barrier signal was routed into the VETO route and passed to a PDP-11 computer. Otherwise, if the MBD time delay expired without a conversion of the TAC ADC, the signal was passed on to the computer in the default NO VETO route. With appropriate delays for the START and STOP signals, it was possible to place the prompt peak in the TAC time spectrum at a nominal position of $5\ \mu\text{s}$, leaving $70\ \mu\text{s}$ available for delayed vetoing. To keep the accidental veto rate small, it was necessary to use a source with an activity of no more than a few kHz.

One-hour-long runs were commenced about 6 h after the activation. The experiment was terminated after about 40 h when the surface barrier detector succumbed to the effects of HF poisoning. Finally, the source was recounted with the Ge(Li) to check for possible long-lived contaminants.

C. Results

The surface barrier spectra for the VETO and NO VETO routes collected during the first 7 h and last 7 h are displayed in Fig. 5. Hereafter, we shall refer to these four spectra as VET(A7), NOV(A7), VET(Z7), and NOV(Z7), respectively. The centroids of the various conversion line peaks were identifiable and remained constant in energy throughout the experiment. From the K215, K332, and K443 lines we obtained an energy calibration and measured the detector resolution to be about 12.8 keV FWHM. This resolution was not good enough to resolve the conversion lines of the L, M, and higher shells. A correction for energy loss through the N_2 gas (approximately 5 keV for the K215 line) was included so that the energy scale (2.97 keV/channel) in Fig. 5 represents the electron energy actually deposited in the surface barrier detector. The LM57-LM93 and LM93-K215 valleys each had a width of 5 channels or 15 keV.

The TAC spectra from the first and last 7 h, TAC(A7) and TAC(Z7), are shown in Fig. 6. The prompt peak had a width of 200 ns and decayed away with a predominant 5.5-h half-life. The delayed β - γ coincidences to the right of the prompt peak persisted throughout the course of the experiment and had a measured slope that matched the ^{181}Hf ($17.8\ \mu\text{s}$, $\frac{1}{2}^+$) activity. In TAC(Z7), 30% of all

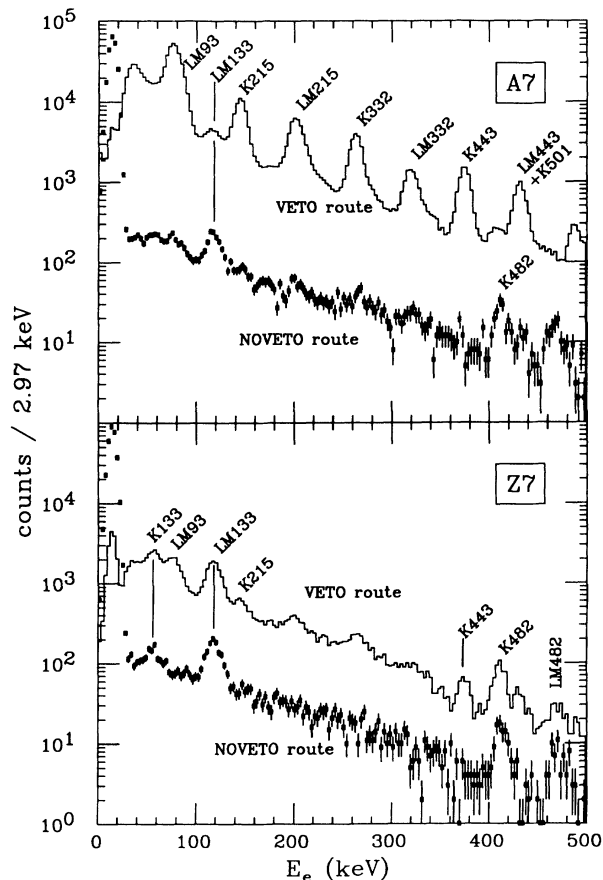


FIG. 5. Routed surface barrier electron energy spectra. Shown are spectra accumulated in the first 7 h (A7) and last 7 h (Z7) of the 36-h experiment.

the TAC events were attributable to this 17.8- μs delayed component. The TAC was calibrated with a pulser in the experimental setup. The TAC "livetime" was measured to be $75.4 \pm 0.2\ \mu\text{s}$. If the TAC received a STOP signal during this time (VETO event), the total MBD dead-time was $94 \pm 1\ \mu\text{s}$. If no STOP signal was received, the MBD dead-time averaged $137\ \mu\text{s}$. The fraction of NO VETO events accidentally routed into the VETO route dropped from 6% to 3% during the course of the experiment.

Since the NaI array had an overall efficiency of 99% for vetoing $^{180}\text{Hf}^m$ conversion electrons, the 5.5-h component of the decay curve given by the TAC STOP signal yielded the absolute $^{180}\text{Hf}^m$ activity. From a fit to this curve, the total number of $^{180}\text{Hf}^m$ decays in the standard A7 set of runs was measured to be $N_0(\text{A7}) = 5.47 \times 10^6$ events.

The Ge(Li) spectra of the activated sample proved it to be very pure. We found γ -ray activities due to the known Hf isotopes, and a small trace of ^{24}Na contamination. At the conclusion of the experiment, we produced a ^{24}Na source by activating a few mg of Na_2CO_3 at the UW reactor. We acquired a spectrum of this β - γ source in the same geometry and setup as above. The small correction for this ^{24}Na contamination is described in Sec. III.

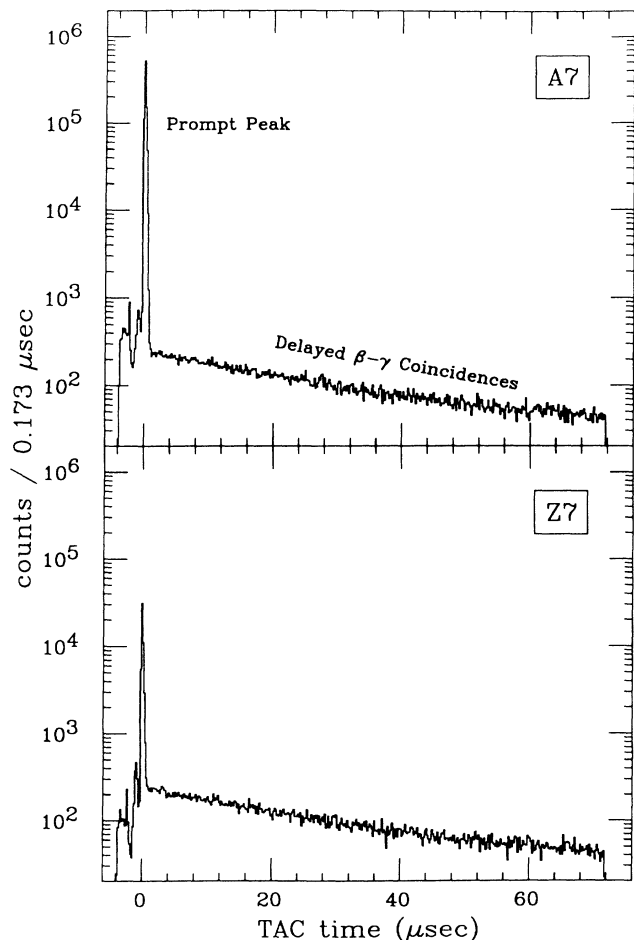


FIG. 6. TAC time spectra between surface-barrier electron events (STARTS) and NaI gamma events (STOPS). The prompt peak has a predominant 5.5-h component while the tail to the right persists with a long half-life. The time slope of the tail matches the 17.8- μ s half-life of the metastable state in the decay of ^{181}Hf .

III. ANALYSIS

A “first” limit on the beta branching ratio f_β was established by taking the ratio of counts on either side of the $LM93$ peak in the NOV(A7) spectrum to the strength of the $LM93$ line in the corresponding VET(A7) spectrum. Using the normalized shape of a 214-keV endpoint beta spectrum for an allowed transition as given by Konopinski [45], we obtained $f_\beta \leq 1.3\%$. This “first” limit does not include any subtractions other than the implicit rejection due to the NaI NO VETO routing. It is already an improvement over Gallagher’s limit of 3.8% and underscores the advantage of our technique.

A. NaI veto

We define the term “rejection factor” to be a ratio of VETO-route electron events to NO VETO route events. We can express the rejection factor, F_{rej} , for the ek th conversion electron of the i th transition in terms of the

probability $P_{\text{NO VETO}}$ for *not* vetoing the set of γ rays in coincidence with it:

$$F_{\text{rej}} = \left[\frac{1 - P_{\text{NO VETO}}}{P_{\text{NO VETO}}} \right]. \quad (7)$$

If the total efficiency $\epsilon_{\text{NaI}}(E_\gamma)$ with which the NaI array registers a single γ event with energy E_γ is known, then

$$P_{\text{NO VETO}}(ek, i) = \delta_{ek, i} \sum_{\text{BP}} f_{\text{BP}} \delta_{i, j} \sum_{\{j\}} P_{\text{config}}\{j\} P_{\text{no veto}}\{j\} \quad (8)$$

with

$$P_{\text{config}}\{j\} = \prod_j \left[\frac{\delta_{\gamma, j} + \delta_{eK, j} \alpha_K(j) + \delta_{eL, j} \alpha_L(j)}{1 + \alpha_K(j) + \alpha_L(j)} \right]$$

and

$$P_{\text{no veto}}\{j\} = \prod_j [1 - \delta_{\gamma, j} \epsilon_{\text{NaI}}(E_j) - \delta_{eK, j} \epsilon_{\text{NaI}}(E_K)],$$

where $\delta_{a, b}$ is a Kronecker-delta-like function between the sets a and b

$$\delta_{a, b} = \begin{cases} 1 & \text{if } a \in b, \\ 0 & \text{if } a \notin b \end{cases}$$

and α_k is the internal conversion coefficient for the k th atomic shell. The first sum in Eq. (8) is taken over all possible branch paths BP from the parent radioactivity (isomer) to the daughter (ground state) and includes the sell $\{j\}$ of transitions for each path with intensity f_{BP} . The second sum is taken over all possible permutations of the set $\{j\}$ of electron and gamma transitions. The rejection due to K x rays is explicitly included in Eq. (8).

It is evident from Eqs. (7) and (8) that each conversion line possesses its own (different) rejection factor. Therefore we cannot simply subtract a scaled-down VETO route spectrum from the NO VETO route spectrum to search for the underlying beta continuum. Furthermore, the total efficiency of the surface barrier detector is large (16.0%) and we must consider sum lines. Since the collection of a sum line event requires the conversion of two transitions in the $^{180}\text{Hf}^m$ cascade, there will be one less γ ray available for vetoing, and thus a smaller rejection factor. We shall perform a proper subtraction of the conversion electron spectrum later in Sec. III F.

B. ^{181}Hf subtraction

Since the half-lives of the multicomponent decay spectra are well known, a mechanistic approach can be used to subtract the long-lived ^{181}Hf activity from the short-lived $^{180}\text{Hf}^m$ activity. The composite electron energy spectrum $N_i(E)$ for a particular run i can be written in terms of a number j_{max} of “pure” energy spectra $\tilde{N}_j(E)$ with known half-lives $t_{1/2} = \ln 2 / \lambda_j$,

$$N_i(E) = \sum_{j=1}^{j_{\text{max}}} f_{ij} \tilde{N}_j(E) \quad (9)$$

where

$$f_{ij} = f_{\text{live}}(i) e^{-\lambda_j t_1(i)} (1 - e^{-\lambda_j [t_2(i) - t_1(i)]})$$

is just the fraction of the j th “pure” activity in the i th time window $(t_1(i), t_2(i))$ relative to the spectrum which could be obtained in the time interval $(0, \infty)$. Note that $\tilde{N}_j(E)$ is normalized as “detectable” events in the absence of electronic dead times. If spectra in j_{max} separate time windows (or runs) are accumulated, the square fraction matrix can be inverted to obtain the pure spectral components as a linear combination of the experimental runs:

$$\begin{pmatrix} \text{VET}(5.5 \text{ h}) \\ \text{NOV}(5.5 \text{ h}) \\ \text{VET}(42\text{d}) \\ \text{NOV}(42\text{d}) \end{pmatrix} = \begin{pmatrix} 1.000 & -0.065 & -1.017 & 0.047 \\ 0 & 1.065 & 0 & -0.065 \\ -0.026 & 0.002 & 1.017 & -0.046 \\ 0 & -0.028 & 0 & 1.063 \end{pmatrix} \begin{pmatrix} \text{VET}(A7) \\ \text{NOV}(A7) \\ \text{VET}(Z7) \\ \text{NOV}(Z7) \end{pmatrix} \quad (11)$$

The matrix has been normalized so that $\text{VET}(5.5 \text{ h}) = \text{VET}(A7) - \{\text{other spectra}\}$. The remaining spectra represent their expected contribution to the first 7 h. This allows us to compare the $\text{VET}(A7)$ and $\text{NOV}(A7)$ spectra with their “subtracted” counterparts.

The resultant spectra are shown in Fig. 7. All of the $^{180}\text{Hf}^m$ lines have canceled out in $\text{VET}(42 \text{ d})$ and $\text{NOV}(42 \text{ d})$. What appears to be a residual of the $LM133$ line in $\text{VET}(5.5 \text{ h})$ is, in fact, the sum peak of the $LM93 + LM57$ conversion lines. More importantly, the ^{181}Hf $LM133$ and $K482$ line have canceled out to within statistics in $\text{NOV}(5.5 \text{ h})$. Subtraction of the contaminant $LM133$ and $K133$ lines allows the $LM93$ and $K215$ line to stand up and be counted. The continuum intensity has been substantially reduced without “oversubtraction.” In the two valleys where we can look with the greatest sensitivity for the 214-keV-end-point β continuum, the number of counts has been reduced by about 60% to 405 ± 45 and 185 ± 34 counts, respectively. If these counts were due entirely to the 5.5-h beta spectrum, then $f_\beta \approx 0.7\%$.

To this point, we have only used the “inner” and “outer” runs, or about 30% of our data. To check the validity of this subtraction, we examined decay curves in detail. Properly normalized decay curves were generated by dividing the number of counts in an energy window of a given spectrum for a given run by the duration of the run (in hours) times the route-specific live-time fraction. The run data were then fit with the sum of two decaying exponentials. The decay curve of any energy window in the surface barrier VETO-route spectrum (or of any time window in the TAC spectrum) was well fit by allowing only the magnitudes of the 5.5-h and 42.4-d half-life components to vary. Figure 8(a) shows two such fits with $\chi^2_\nu = 1.8$ and 1.5 to VETO-route events—above a threshold energy of 100 keV, and falling in the $LM57$ - $LM93$ window—respectively.

In contrast, the NO VETO route fits for the same energy windows in Fig. 8(b) have relatively poor chi squares. Several runs have higher count rates than statistical fluctuations would allow. For example, the low-energy

$$\tilde{N}_j(E) = \sum_{i=1}^{j_{\text{max}}} f_{ij}^{-1} N_i(E). \quad (10)$$

The various rate- and route-dependent dead times associated with the TAC suggest separate treatment of the NO VETO and VETO routes. When a correction for accidental vetoing (which weakly “couples” the NO VETO fraction matrix to the VETO fraction matrix) is included, we obtain the “pure” spectral components for the $t_{1/2} = 5.518 \text{ h}$ and 42.4 day half-lives in the VETO and NO VETO routes:

count-rate of the eighth data point was two times greater than the rates of its neighbors, suggestive of an intermittent “noise flash” problem. Possible mechanisms resulting in sudden increases in the NO VETO-route count rate

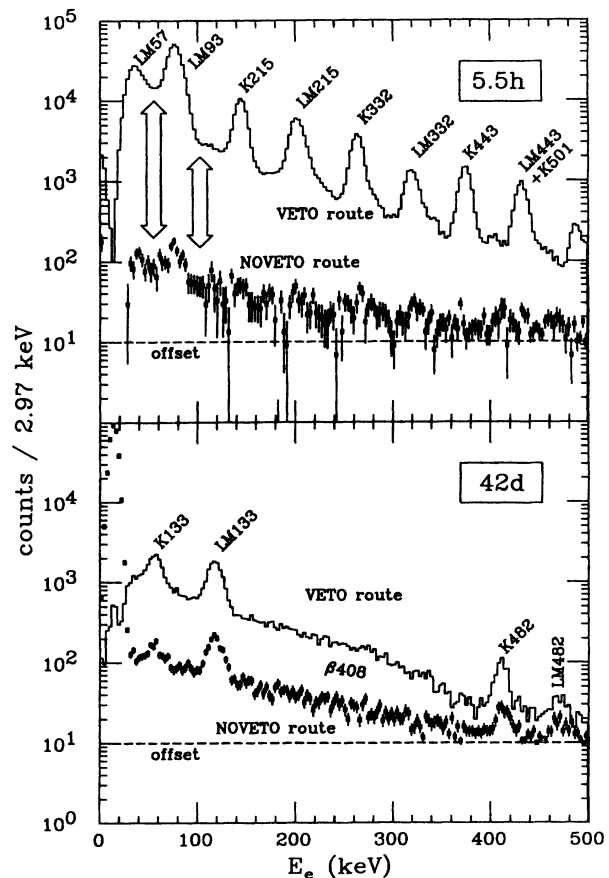


FIG. 7. Subtracted components of the routed surface-barrier electron energy spectra. An offset of 10 counts/channel is added to show that there is no “oversubtraction.” Arrows in the 5.5-h spectrum mark the two “valleys” between the peaks where we searched for the 214-keV-end-point beta spectrum.

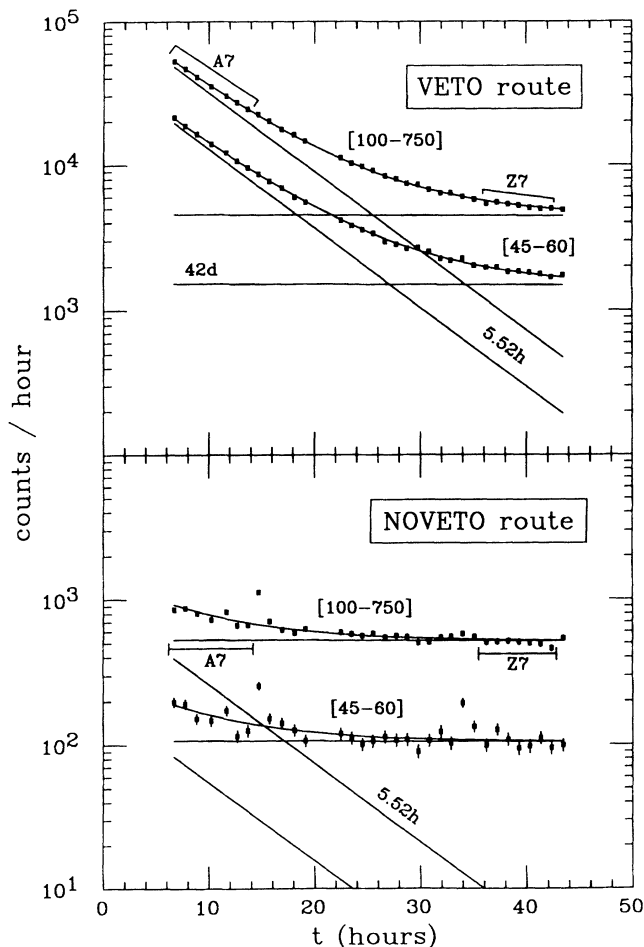


FIG. 8. Decay curves of various energy windows for the surface barrier spectra. Shown are fits to the $LM57$ - $LM93$ valley (45–60 keV) and above the $LM93$ line (100–750 keV) in both the VETO and NO VETO routes.

are (1) break downs in the surface barrier detector, and (2) time variations in the overall NaI veto efficiency.

One suspected source of intermittent random noise is HF vapor poisoning of the surface barrier detector. It was noted that there was an interruption of the N_2 purge prior to the eighth run. Examination of the residual energy spectrum of this run (formed by subtracting one-half each of the 7th and 9th runs) showed that the noise was distributed approximately exponentially, extending to several hundred keV in energy and that the $LM93$ and $LM133$ peaks statistically canceled to zero. It is worthy of note that the shape of the 408-keV-end-point beta continuum in the NOV(42 d) spectrum matched the shape in the VET(42 d) spectrum, which we know must be free from the “noise flash” spectrum. Since the Z7 runs were chosen in a nominally flat (only small deviations from the norm) time region. This observation limits the size of a low-energy “noise flash” component which might have been oversubtracted from the NOV(A7) spectrum.

The NO VETO count rate is sensitive to small changes in the NaI veto efficiency (due to gain changes in the phototubes, for example). If the increase in NO VETO rate arises from variations in the veto efficiency, then known

electron peaks should scale with the “noise” continuum. As described above, this was shown not to be the case. Furthermore, the complete cancellation without oversubtraction of the $LM133$ peak in the NOV(5.5 h) spectrum provides reassurance regarding long-term efficiency drifts.

A two-component decay curve (with fixed 5.5-h and 42-d half lives) was fit to the energy-window counts over a full set and several subsets of all the runs. As expected, the set of points consisting of the first 7 and last 7 runs yielded a 5.5 h component that matched the number of counts obtained by integrating the same window in the NOV(5.5 h) spectrum. As shown in Table IV, the 5.5-h component never falls more than one statistical standard deviation from this value, even when the full data set is included. We measured the variance in the number of counts for the set of fits to be 22 and 10 counts for the two valleys. We use these one-sigma values as a measure of an additional statistical uncertainty inherent in the ^{181}Hf subtraction due to our “noise flash” problem.

C. ^{24}Na subtraction

The electron spectrum of ^{24}Na is a featureless continuum due to its 1390-keV-end-point beta spectrum. In our experimental geometry, we measured the intensity fall by a factor of 2.5 between 100 and 600 keV. Two coincident high-energy gamma rays (1369 and 2754 keV) resulted in a rejection factor $F_{\text{rej}}=10$. The matrix of Eq. (11) only partly subtracts out the intermediate half-life (15.02 h) ^{24}Na component. We normalized the experimentally measured ^{24}Na spectrum to the A7 set of runs using the Ge(Li) counts of the 1369-keV gamma line.

Below 100 keV, the VETO route has a ^{24}Na contribution of 18 counts/2.97 keV, which is less than 1% of the valley continuum intensity in Fig. 7. In the $LM57$ - $LM93$ and $LM93$ - $K215$ valleys of the NO VETO route, the ^{24}Na strength was 2.2 and 2.0 counts/2.97 keV corresponding to 11 and 10 total counts, respectively. The ^{24}Na contribution was only significant above 500 keV where it accounted for 50% of the measured continuum strength between the known sum peaks. We verified that decay curves for high-energy windows possessed a 15-h component. We calculated that the continuum associated with the sum peaks was an order of magnitude less than the experimentally measured continuum at these energies. To conservatively include the possibility that the geometry was not well reproduced, we consider the measurement described above to be a *lower* bound on the ^{24}Na contribution. The upper bound is then defined by the high-energy continuum limit and we assign the NO VETO valley contributions to be $16 \pm 1 \pm 5$ and $15 \pm 1 \pm 5$ counts in Table IV.

D. Electron detector response function

Monoenergetic electrons from a discrete-line source can Møller scatter both into and out of a detector, depositing less than their full energy to produce a featureless backscatter tail [46]–[51]. Further, the ratio of total scattered events to peak events is approximately a con-

TABLE IV. Accounting of surface-barrier electron counts in the energy valleys on either side of the LM93 peak. Equivalent values for f_β in the right-hand columns are traced through the two subtractions.

Spectrum/Run	Valley: Energy (keV):	Window		f_β	
		I	II	I	II
		LM57-LM93 [47.6-62.4] (counts)	LM93-K215 [95.0-109.9] (counts)	(%)	(%)
VET(A7)		88000±300	20730±150		
VET(5.5 h)		75750±320	16360±160		
NOV(A7)		1091±33	585±24	1.50	1.87
NOV(5.5 h)		405±45	185±34	0.56	0.59
NO VETO-route time-decay curve fits: 5.5 h component					
All 33 runs		420±39	186±29		
Less 8th run		394±39	171±29		
A7 + Z7		408±43	197±32		
Odd No. runs		392±51	186±39		
Even No. runs		455±60	184±43		
Variance of Set		409±22	183±10		
NOV(5.5 h)		405±50	185±36	0.56	0.59
^{24}Na Contaminant		16±6	15±6		
Absolute β normalizations					
1% β_{214} (Konopinski)		6460	3750		
1% β (EGS4)		584	348	0.80	1.11
1% β (LM93 Convol.)		866	367	1.19	1.17
1% β (K215 Convol.)		725	313	1.00	1.00
1% β (K392 Convol.)		792	346	1.09	1.10
Adopted 1% β_{214}		725(20%)	313(20%)	1.00	1.00
Global fit to VET(5.5 h): LM93 scaled ($\chi^2_\nu=28.0$)					
<i>singles</i> less LM93		19 768	8 493		
LM93 Line		52 000	1 957		
<i>doubles</i>		3 438	7 807		
^{24}Na Contam.		150	139		
Fit sum:		73 355	18 396		
Deficit counts		395	-2 036		

stant with respect to the incident electron energy. For a well-collimated beam of monoenergetic electrons in vacuum and perpendicularly incident to a Si detector, the fraction of backscattered events has been experimentally determined to be 13.4% [51]. The geometry used in our experiment is more extreme since the surface barrier detector subtends a substantial fraction of 4π (10.7%) and numerous scattering media exist close to the detector including the centimeter of nitrogen gas through which the electrons must pass. Most electrons impinge on the detector surface at oblique angles (up to 45°) with increased likelihoods that they will scatter out.

To experimentally determine the electron response functions of our Si surface barrier detector, two conversion line sources were prepared and placed in the same geometry as the $^{180}\text{Hf}^m$ source. Both ^{113}Sn and ^{139}Ce decay by electron capture to the first excited states of ^{113}In

and ^{139}La at 391.7 and 165.8 keV, respectively. The ^{113}Sn source was found to be contaminated with the β emitter ^{125}Sb . The ^{125}Sb contribution was estimated and subtracted by convoluting the theoretical β spectrum, normalized by the Ge(Li)-measured 427.9-keV gamma strength, with the first-order ^{113}Sn response function. The resultant ^{113}Sn spectrum is shown in Fig. 9(a). If the plateau between 100 and 300 keV is assumed to continue down to 0 keV, then the total tail-to-peak ratio is 0.91. The ^{139}Ce spectrum shown in Fig. 9(b) was obtained with somewhat poorer resolution. We have subtracted out the strong K x-ray contribution at 34.2 keV to show that the plateau is essentially flat down to the noise threshold. Tests with the ^{139}Ce source demonstrated that the total tail-to-peak ratio was sensitive to the source-to-detector distance.

To augment these experimental measurements of the

TABLE IV. (Continued).

Spectrum/Run	Window		f_β		
	Valley:	I	II	I	II
	Energy (keV):	$LM57-LM93$ [47.6–62.4] (counts)	$LM93-K215$ [95.0–109.9] (counts)	(%)	(%)
Global fit-1 to NOV(5.5 h): No. $\beta214$, $LM93$ unconstrained ($\chi^2_\nu=1.21$)					
<i>singles less LM93</i>		63±6	41		
<i>LM93 line</i>		161±9	6		
<i>doubles</i>		21±3	48		
^{24}Na Contam.		16	15		
Fit 1 sum:		261	110		
Deficit counts		144	75		
Global fit-2 to NOV(5.5 h): $LM93$ scaled ($\chi^2_\nu=1.09$)					
<i>singles less LM93</i>		65±10	42		
<i>LM93 line</i>		84	3		
<i>doubles</i>		14	32		
^{24}Na Contam.		22±5	20		
$\beta214$		234±43	100	0.32	0.32
Fit-2 Sum:		419	197		
Residual $\beta214$ from fit 2		220±55	88±37	0.31	0.28
Global fit 3 to NOV(5.5 h): $LM93$ unconstrained ($\chi^2_\nu=1.05$)					
<i>singles less LM93</i>		52±6	34		
<i>LM93 Line</i>		109±12	4		
<i>doubles</i>		20±3	45		
^{24}Na Contam.		16	15		
$\beta214$		201±33	86	0.28	0.27
Fit-3 sum:		398	184		
Residual $\beta214$ from fit 3		208±52	87±37	0.29	0.28

response function, theoretical spectra were generated with the Electron-Gamma-Shower Monte Carlo code EGS4 [52]. We used a Los Alamos version of the code for cylindrically symmetric geometries and introduced routines for low-energy electrons as suggested by Rogers [53]. As inputs to the EGS4 code, we measured the experimental geometry including all absorbing and scattering media within range of the electrons. The EGS4 code propagated monoenergetic electrons randomly into 4π sr. Spectra of the electron energy deposited in the region defined by the Si medium were accumulated and were then convoluted with a Gaussian to mock up the detector resolution. Simulated electron spectra for ^{113}Sn and ^{139}Ce are displayed in Fig. 9. In general, the EGS4 code successfully reproduced the peak shift due to energy loss and the qualitative shape of the backscatter tail, but failed to yield a large enough tail-to-peak ratio by 15 to 35%. This discrepancy probably springs from difficulties in modeling the precise geometry and in properly accounting for the Møller scattering in the code [52–54]. We further showed through use of the code that backscattering into the Si detector was a strong function of the thickness of the high- Z HfF_4 source. Thus an uneven distribution of source thickness could enhance conversion-line tails. The calculated spectra show a drop off at energies below the experimental low-energy thresh-

old. This is important for summed spectra, which we will discuss in the next subsection.

We used EGS4 code to generate electron spectra for each conversion line listed in Table II and III. For all but the $LM57$ case, $8.2\pm 0.4\%$ of the EGS4 electrons contributed to the “full-energy” peak in the active zone of Si. Another 5.0% of the electrons fell in the backscatter tail, independent of the initial electron energy. To correct for the tail-to-peak ratios actually observed, we rescaled the computed tails up to 7.8% while maintaining their energy distribution. The strong, low-energy $LM93$ line was treated separately. As can be seen in the VETO-route spectrum of Fig. 7, the valley to the left of the $LM93$ peak has an order of magnitude more counts in it than the valley to the right, and must therefore be dominated by the backscatter tail attached to the $LM93$ peak. To simulate the observed plateau-to-peak ratio, we found it necessary to double the calculated tail contribution to a value of 10.0%.

Beta spectra for the expected 214-keV end point allowed transition from $^{180}\text{Hf}^m$ to $^{180}\text{Ta}^m$, and, for the 408-keV-end point, ^{181}Hf decay were generated with EGS4 from a binned “ideal” distribution [45]. However, the *ad hoc* correction to the tail-to-peak ratio should result in a skewed increase in the low-energy component of these beta spectra. We generated three other mock 214-keV-

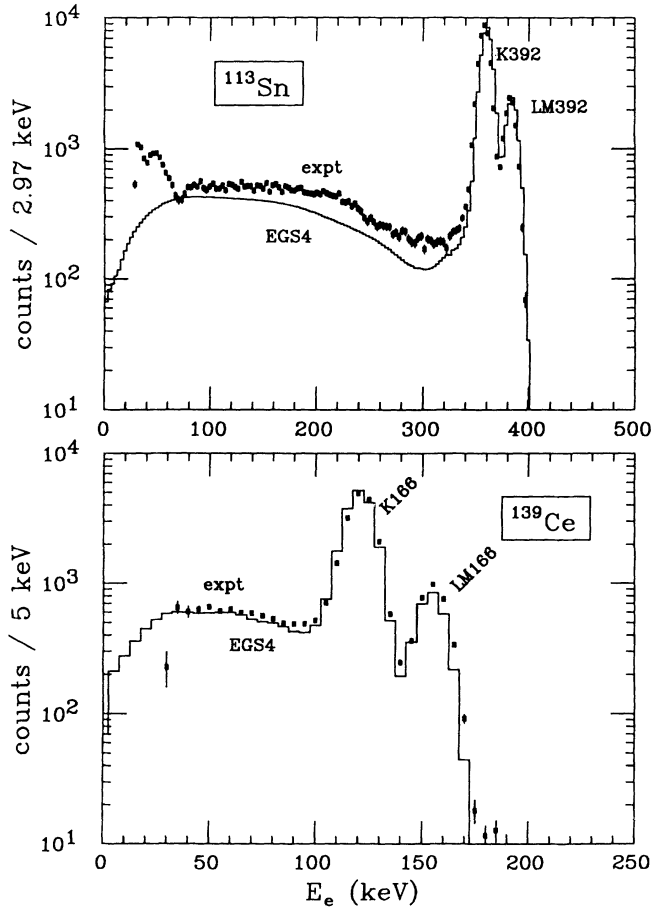


FIG. 9. Conversion-line source spectra for ^{113}Sn and ^{139}Ce . Shown are the experimentally-measured energy spectra and the EGS4-generated response function, smoothed by the 12.8-keV detector resolution.

end-point β spectra by convoluting the ideal spectrum with the response function given by the $LM93$, $K215$, and ^{113}Sn $K392$ lines. These different determinations agreed with each other at the 20% level between 30 and 180 keV. The contributions of each generated β spectrum to the $LM57$ - $LM93$ and $LM93$ - $K215$ valleys defined earlier are given in Table IV, normalized to 1.00% of the total number of $^{180}\text{Hf}^m$ decays in the A7 time bin. We have chosen to use the 1% β spectrum based on the convolution of the $K215$ line which yields to 725 and 313 counts respectively in the $LM57$ - $LM93$ and $LM93$ - $K215$ valleys. We interpret the differences in normalization as a 20% systematic uncertainty which will carry over to the determination of f_β .

E. electron line summing

Since the total efficiency of the surface barrier detector is large (16%), we must consider electron line summing for the high-multiplicity $^{180}\text{Hf}^m$ cascade. We can express the sum-line differential energy spectrum by

$$m_{i\oplus j}(E) = \int_{E_i=0}^E n_i(E_i)n_j(E-E_i)dE_i \quad (12)$$

where $n_i(E_i)$ and $n_j(E_j)$ are the differential energy spectra (response functions) for the i th and j th transitions of the cascade per decay. Note that since the integrated tail-to-peak ratio is nearly 1 for single electron spectrum, the tail-to-summed-peak ratio becomes about 3 for sum-line spectra $n_{i\oplus j}$. The phase-space construction of Eq. (12) is such that if $n_i(E)$ approaches a constant as E goes to 0, then $n_{i\oplus j}(E) \propto E$ for low energies. If $n_i(E) \propto E$, as suggested by the EGS4 modeling, then $n_{i\oplus j}(E) \propto E^3$ at the lowest energies in the sum-line spectrum. Thus the contribution of the sum-line spectra to the lowest-energy valleys (below the $LM93$ peak) must be small compared to higher-energy valleys.

F. Global spectra fits

Response functions $n_i(E)$ were generated for each conversion line in the $^{180}\text{Hf}^m$ spectrum by smoothing the tail-corrected EGS4 model. A *singles* curve was created by first summing the response functions, normalized to the absolute intensities as given in Table II, and then convoluting it with the 12.8-keV detector resolution. A small correction was made for summing out of the *singles* line strength. The full-energy peaks of the VET(5.5 h) spectrum are well-reproduced (to within the uncertainties in the conversion-line magnitudes) by the *singles* curve in Fig. 10 even when the absolute activity of the source is used as the normalization. However, the *singles* curve accounts for less than half of the number of counts in the valleys between the peaks. A properly normalized *doubles* curve was generated by summing each of the possible sum-line combinations $n_{i\oplus j}(E)$ and again convoluting the result with the Gaussian detector resolution. Finally we added the ^{24}Na spectrum, normalized as described earlier. The *singles* and *doubles* curves were globally fit to the VET(5.5 h) spectrum between 40 and 500 keV. As seen in Fig. 10, the *doubles* curve does an excellent job of filling in the valleys and, with the fixed ^{24}Na continuum, well represents the data for energies in excess of the highest-energy single conversion electron. The chi square per degree of freedom (χ^2_ν) for this two-parameter fit equals 30, which means that the average discrepancy between the EGS4-generated theoretical curve and the data is about 10%. Much of the excess chi square exists near the low-energy $LM57$ peak (whose centroid lies below the low-energy noise threshold at 35 keV) where the EGS4 code is of questionable reliability. The fit required a *doubles* component 17% above the absolute normalization. This might be explained by either an inflation of the total detector efficiency (from 16.0% to 18.2%) or of the tail-to-peak ratio or possibly by electron-electron angular correlation. In spite of these problems, the global fit is remarkably good.

For each γ transition listed in Tables II and III, we calculated the total efficiency of the NaI array with the EGS4 code and used Eqs. (7) and (12) to determine rejection factors. These proved to be much larger ($F_{\text{rej}} > 1000$) than the measured values, perhaps due to incomplete light collection in the annular NaI detector. We therefore adjusted the low-energy end of the γ efficiency curve within the "annulus-only" envelope until

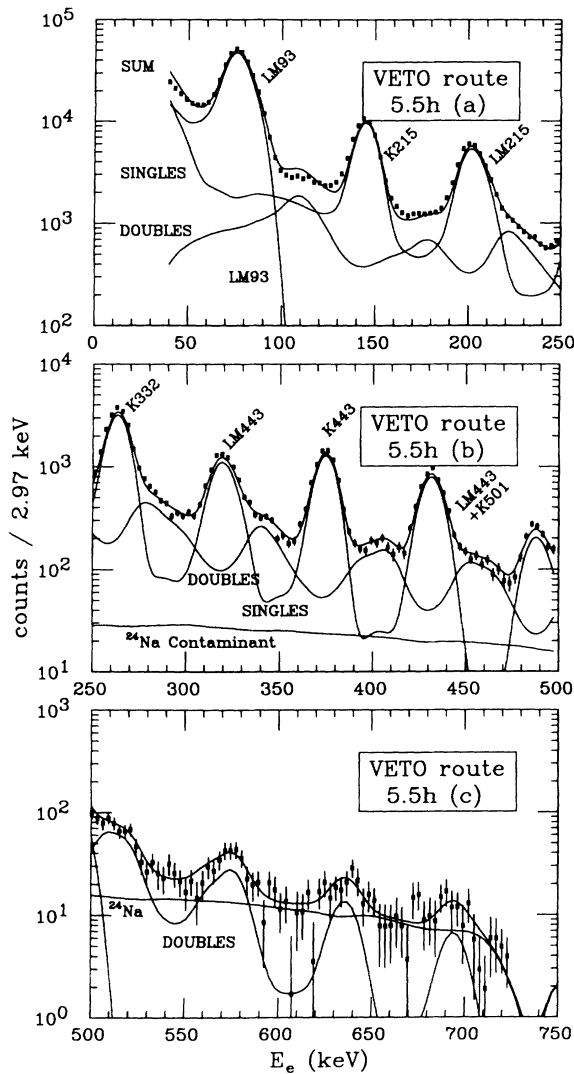


FIG. 10. Global simulation of the $^{180}\text{Hf}^m$ VETO-route electron energy spectrum. General agreement with the data was achieved across the entire spectrum.

the computed NO VETO rejection factors agreed with the measured values of Tables II and III. Simulations of the VET(42 d) and NOV(42 d) spectra are shown in Fig. 11. The LM133 peak is promptly rejected by a factor of 10, due primarily to coincidences with the 482-keV line. Likewise, the beta continuum is rejected by a factor of 8. To mock up the effect of the 17.8 μs half-life, 7% of the 408-keV-end-point beta decays were assigned to be multiplicity = 1 events. To within a normalization factor, the manufactured spectra in Fig. 11 do a reasonably good job of reproducing both the conversion-line and β components of the VETO- and NO-VETO-route spectra. The match is not as good as the VET(5.5 h) simulation, in part because the absolute branching ratios in Table III are not well known.

In the same manner, the $^{180}\text{Hf}^m F_{\text{rej}}$ factors were used to generate *singles* and *doubles* spectra for the NO VETO route. To these were added the β spectra from the ^{24}Na

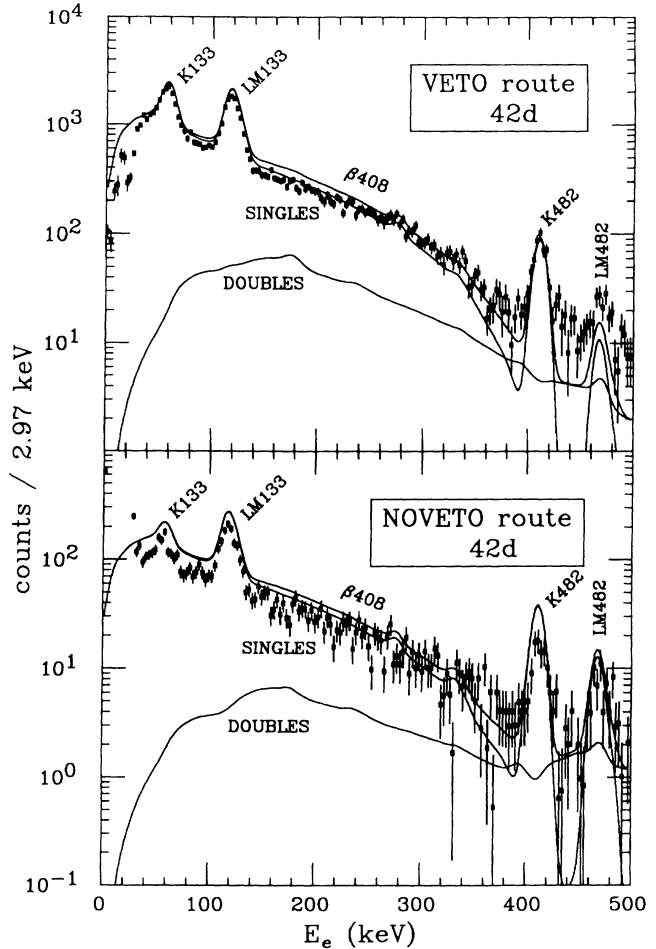


FIG. 11. Global simulation of the ^{181}Hf electron energy spectra in both the VETO and NO VETO routes. Shown are the absolute normalizations given in Table III.

contaminant and $^{180}\text{Hf}^m f_{\beta}$ branch. We then used our chi-square fitting routine to globally fit the sum of these simulated spectra to the NOV(5.5 h) data spectrum between 40 and 720 keV. When the magnitude of the 214-keV-end-point β spectrum was fixed to 0 ($f_{\beta}=0$), the smallest χ^2_{ν} which could be achieved was 1.21 (fit 1 in Fig. 12 and Table IV). If the parent distribution correctly modeled, then the integrated chi-square-probability distribution of this global fit is only $P(>\chi^2_{\nu})=1.7\%$ due to a substantial discrepancy (40%) in the low energy valleys. When a positive β spectrum was added as a fitting parameter, the χ^2_{ν} dropped to a value of 1.08 [$P(>\chi^2_{\nu})=15\%$]. Examination of this fit (fit 2 in Table IV) showed that the β spectrum absorbed fully half of the counts in both the LM57-LM93 and LM93-K215 valleys. To account for the possibility that an improper rejection factor has been used for the LM93 line relative to the other NO VETO lines, the magnitude of the *singles* LM93 peak with its associated tail was allowed to vary independent of the other *singles* and *doubles* lines. In the resulting fit 3 (Fig. 12 and Table IV) the LM93 contribution increased (60% relative to the other *singles* lines) without significantly draining the beta strength. In this fit, the χ^2_{ν} fell to 1.04

$[P(>\chi^2_v)=30\%]$.

Both fit 2 and fit 3 statistically agreed with each other. Half of the counts in each valley belonged to the 214-keV-end-point beta spectrum. Concentrating on the $LM57-LM93$ valley, about 100 counts of the 405 ± 50 could be attributed to the nearby $LM93$ line. Another 50 counts could be explained by the backscatter tails of other *singles* spectra. Only 20 counts came from the *doubles* spectrum. As discussed earlier, the ^{24}Na contribution amounted to only 16 counts. This left a residue of over 200 counts which was fully accounted for by the globally fit β spectrum. Since the NOV(5.5 h) valleys contained both statistical and systematic errors, we used the average of the beta residual (defined to be the difference between the data and the fit values less the beta component) to obtain

$$N_\beta(LM57-LM93)=215\pm 55 \text{ counts ,}$$

$$N_\beta(LM93-K215)=87\pm 37 \text{ counts .}$$

Using the adopted 1% β_{214} normalizations from Table

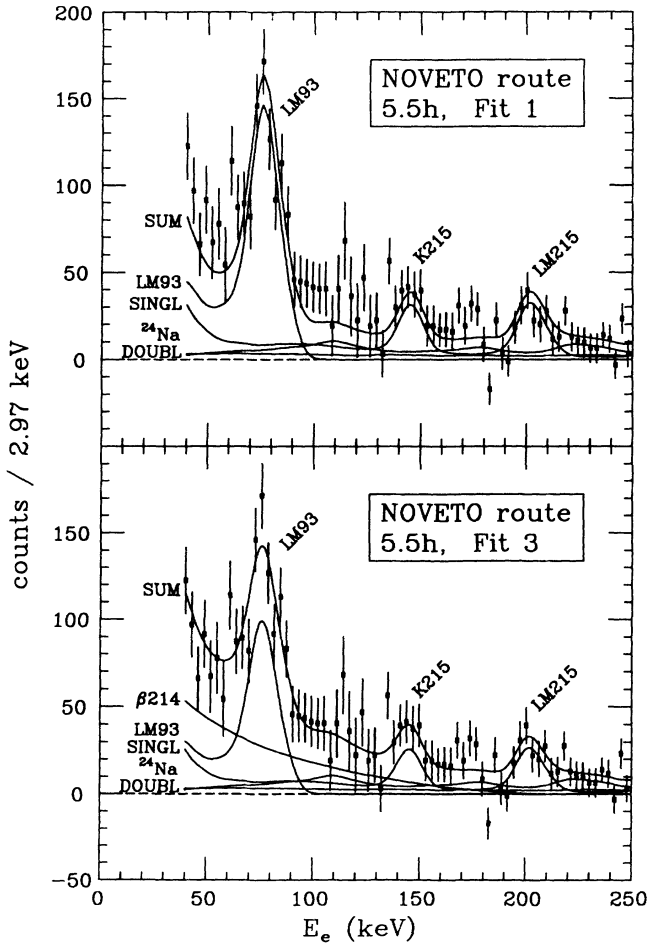


FIG. 12. Global simulations of the $^{180}\text{Hf}^m$ NO VETO-route electron energy spectrum. In fit 1, we assume zero β spectral strength and allow the $LM93$ strength to vary. A large (40%) discrepancy between the data and the fit is apparent in the low-energy valleys. In fit 3, an excellent fit is obtained when the β component contributes about 50% to the $LM57-LM93$ and $LM93-K215$ valleys.

IV, we can write down the laboratory beta branching ratio as

$$f_\beta(LM57-LM93)=(0.30\pm 0.07\pm 0.06)\% ,$$

$$f_\beta(LM93-K215)=(0.28\pm 0.12\pm 0.06)\% ,$$

where we have included the 20% normalization uncertainty as a systematic error.

IV. DISCUSSION AND CONCLUSION

We have measured the direct isomer-to-isomer β -decay branch of $^{180}\text{Hf}^m$ to $^{180}\text{Ta}^m$ by (1) vetoing electron events from a Si surface barrier detector in coincidence with gamma rays detected in a 4π NaI array, (2) subtracting the $t_{1/2}=42$ d ^{181}Hf component from the predominant 5.5-h $^{180}\text{Hf}^m$ component, and (3) subtracting the conversion line component from the electron energy spectrum. Our final result, statistically combined over the two valleys,

$$f_\beta=(0.29\pm 0.05\pm 0.06)\%$$

is more than a factor of 10 times smaller than the only previously published limit [30]. The statistical and systematic uncertainties are conservatively estimated. Our measurement of f_β corresponds to a partial half-life of 76 d and an isomer-to-isomer $\log ft$ value of 6.4 ± 0.2 . This is consistent with an allowed-hindered β transition and suggests that the structure of $^{180}\text{Hf}^m$ is a nearly pure broken-proton configuration. (Upon completion of our effort, we learned of an experiment by Barden who measured $f_\beta=0.22\pm 0.05\%$ [55]. This value is in statistical agreement with our results.)

We summarize the status of the Beer and Ward model for the production of ^{180}Ta in Fig. 13. The s - and r -process contributions to the solar-system abundance of $^{180}\text{Ta}^m$ are used as the abscissa and ordinate. If the abundance of $^{180}\text{Ta}^m$ is fully accounted for by neutron capture processes, then it can be plotted somewhere on the $N_s + N_r = N_\odot$ line connecting the points (0,1) and (1,0). We use Eqs. (5) and (6) to write down linear solutions for laboratory values of f_m and f_β and overlay this grid on the abundance coordinates. Our measurement of f_β with its associate uncertainties coupled with our previous measurement of f_m defines region (a) in Fig. 13. If we let the enhancement factor of Eq. (4) vary over the range of values allowed by possible s -process environmental conditions for both the s and the r processes, the larger region (b) is formed. Finally, the remaining uncertainties in the nuclear and geophysical inputs to Eqs. (1) and (6) are acknowledged by expanding the $N_s + N_r = N_\odot$ line into region (c).

The lack of an overlap between region (a) and the $N_s + N_r = N_\odot$ line, and even between the less-restrictive regions (b) and (c), suggests that another mechanism is needed to explain the solar-system abundance of $^{180}\text{Ta}^m$. Between a fourth and a half of $N_\odot(^{180}\text{Ta}^m)$ can be produced, almost entirely in the s process. However, all of our calculations [Eqs. (1)–(6)] have implicitly assumed that the isomers of ^{180}Hf and ^{180}Ta will not be rapidly equilibrated with their respective ground states via pro-

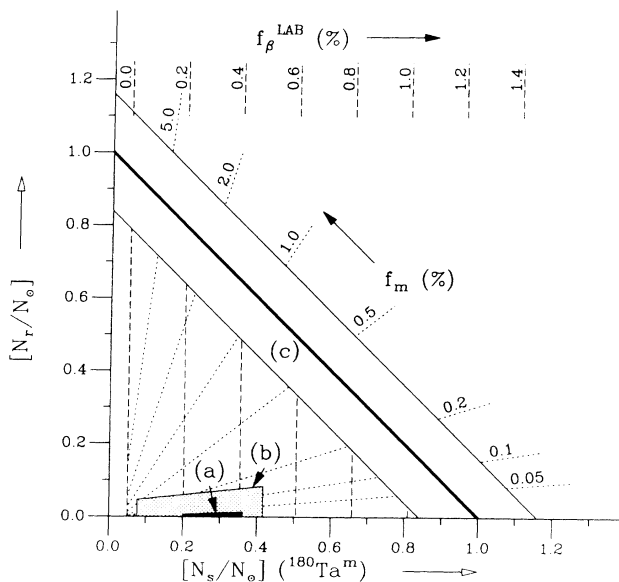


FIG. 13. Status of the Beer and Ward theory for the production of ^{180}Ta . Fractions of the observed solar-system abundance of $^{180}\text{Ta}^m$ produced in the s and r processes are used as the abscissa and ordinate of the plot. Superimposed are solutions to Eqs. (5) and (6) for laboratory-measured values of f_β and f_m assuming nominal s -process environmental conditions. Region (a) represents 68% confidence limits on our experimental measurements. Region (b) further includes the possible range of enhancement factors F_s^{enh} defined in Eq. (4) for other plausible stellar conditions in the neutron-capture processes. Region (c) represents uncertainties in the remaining input physics (abundances and neutron cross sections). Lack of an overlap between region (a) and the $N_s + N_r = N_\odot$ line, and even between the less-restrictive regions (b) and (c), force us to conclude that the Beer and Ward model cannot quantitatively account for all of the $^{180}\text{Ta}^m$ found in nature.

to deexcitation in the hot s -process environment. Such an eventuality would block the production of and/or lead to the destruction of any $^{180}\text{Ta}^m$ made via the Beer and Ward path. Laboratory experiments have not located any *low-lying* (≤ 2.5 MeV) threshold states which might

form a direct communication link between the isomeric and ground states in ^{180}Ta [56-59]. The case for photo-deexcitation of $^{180}\text{Hf}^m$ is unexplored. On the basis of a theoretical investigation [60], we believe that much of the $^{180}\text{Ta}^m$ created *will* be equilibrated with the short-lived ground state unless the production occurs at rather low temperatures ($kT < 18$ keV). We thus conclude that the Beer and Ward mechanism fails to account for the sparse abundance of ^{180}Ta in the Universe.

There is no lack of alternative production schemes however. Yokoi and Takahashi have proposed another s -process branch involving excited-state β decay from ^{179}Hf to ^{179}Ta ($t_{1/2} = 1.7$ yr) followed by neutron capture [10]. Hainebach, Schramm, and Blake have considered interstellar spallation [61], while Harrison invokes a Γ process that uses preequilibrated high-energy gammas as a source for photodisintegration reactions [62,63]. Recently, Woosley *et al.* have incorporated $^{180}\text{Ta}^m$ nucleosynthesis in their description of the ν process [64]. The observed abundances of $^{180}\text{Ta}^m$ and ^{180}W probably place severe constraints on the site of the s -process and other stellar (and interstellar) environments [10]. Until the experimental challenges are met, however, the origin of $^{180}\text{Ta}^m$ must remain an unsolved and tantalizing puzzle.

ACKNOWLEDGMENTS

The authors gratefully acknowledge the assistance of Pat Miller and Deloss Fry for the reactor activations, K. Takahashi for performing the bound-state β -decay calculations, and Richard Seymour for software help. We wish to thank Hans Bichsel, Dave Bodansky, and Tom Trainor for helpful advice, and R. W. Kavanagh for carefully reading the manuscript. One of us (S.E.K.) would also like to acknowledge the hospitality extended by the faculty and staff of the Kellogg Radiation Laboratory at the California Institute of Technology where the final manuscript was prepared. This work was supported in part by the U.S. Department of Energy at the University of Washington under Contract No. DEAC06-81ER40048 and at LBL under Contract No. DEAC03-76SF00098.

[1] *Table of Isotopes*, 7th ed., edited by C. M. Lederer and V. S. Shirley (Wiley, New York, 1978).
 [2] F. A. White, T. L. Collins, Jr., and F. M. Rourke, *Phys. Rev.* **97**, 566 (1955).
 [3] F. A. White, T. L. Collins, and F. M. Rourke, *Phys. Rev.* **101**, 1786 (1956).
 [4] E. Warde, R. Seltz, G. Costa, D. Magnac, and C. Gérardin, *Phys. (Paris)* **1**, L1 (1978).
 [5] B. Burghardt, R. Harzer, H. J. Hoeffgen, and G. Meisel, *Phys. Lett.* **92B**, 64 (1980).
 [6] K. S. Sharma, R. J. Ellis, V. P. Derenchuk, and R. C. Barber, *Phys. Lett.* **91B**, 211 (1980).
 [7] J. B. Cummings and D. E. Alburger, *Phys. Rev. C* **31**,

1494 (1985).
 [8] H. Beer and R. A. Ward, *Nature* **291**, 308 (1981).
 [9] H. Beer and R. L. Macklin, *Phys. Rev. C* **26**, 1404 (1982).
 [10] K. Yokoi and K. Takahashi, *Nature* **305**, 198 (1983).
 [11] E. Browne, *Nucl. Data Sheets* **52**, 127 (1987).
 [12] S. E. Kellogg and E. B. Norman, *Phys. Rev. C* **31**, 1505 (1985).
 [13] D. D. Clayton, W. A. Fowler, T. E. Hull, and B. A. Zimmerman, *Ann. Phys.* **12**, 331 (1961).
 [14] P. A. Seeger, W. A. Fowler, and D. D. Clayton, *Astrophys. J. Suppl.* **11**, 121 (1965).
 [15] D. D. Clayton, *Principles of Stellar Evolution and Nucleosynthesis* (Univ. of Chicago Press, Chicago, 1983).

- [16] F. Käppeler, H. Beer, K. Wisshak, D. D. Clayton, R. L. Macklin, and R. A. Ward, *Astrophys. J.* **257**, 821 (1982).
- [17] E. Anders and M. Ebihara, *Geochim Cosmochim. Acta* **46**, 2363 (1982).
- [18] Z. Y. Bao and F. Käppeler, *At. Data Nucl. Data Tables* **36**, 411 (1987).
- [19] A. G. W. Cameron, in *Essays in Nuclear Astrophysics*, edited by C. A. Barnes, D. D. Clayton, and D. N. Schramm (Cambridge University Press, Cambridge, 1982), p. 23.
- [20] M. J. Harris, *Astrophys. Space Sci.* **77**, 357 (1981).
- [21] J. A. Holmes, S. E. Woosley, W. A. Fowler, and B. A. Zimmerman, *At. Data Nucl. Data Tables* **18**, 305 (1976).
- [22] R. L. Macklin, *Nucl. Sci. Eng.* **86**, 362 (1984).
- [23] R. L. Macklin, *Nucl. Sci. Eng.* **85**, 350 (1983).
- [24] B. Strömgren, *Z. Astrophys.* **4**, 118 (1932).
- [25] J. N. Bahcall, *Phys. Rev.* **124**, 495 (1961).
- [26] K. Takahashi, private communication (1984).
- [27] K. Takahashi and K. Yokoi, *Nucl. Phys.* **A404**, 578 (1983).
- [28] G. J. Mathews and R. A. Ward, *Rep. Prog. Phys.* **48**, 1371 (1985).
- [29] S. E. Kellogg and E. B. Norman, *Phys. Rev. C* **34**, 2248 (1986).
- [30] C. J. Gallagher, M. Jorgenson, and O. Skilbreid, *Nucl. Phys.* **33**, 285 (1962).
- [31] W. Eschner, W.-D. Schmidt-Ott, K. L. Gippert, E. Runte, H. Beer, G. Walter, R. Kirchner, O. Klepper, E. Roeckl, and D. Schardt, *Z. Phys. A* **317**, 281 (1984).
- [32] K. T. Lesko, E. B. Norman, D. M. Moltz, R. M. Larimer, S. G. Crane, and S. E. Kellogg, *Phys. Rev. C* **34**, 2256 (1986).
- [33] E. Runte *et al.*, *Z. Phys. A* **328**, 119 (1987).
- [34] S. G. Nilsson, *Kgl. Dan. Vid. Selsk. Mat. Fys. Medd.* **29**, no. 16 (1955).
- [35] A. J. Rassej, *Phys. Rev.* **109**, 949 (1958).
- [36] C. J. Gallagher and H. L. Nielsen, *Phys. Rev.* **126**, 1520 (1962).
- [37] P. Manfrass, W. Andrejtscheff, P. Kemnitz, E. Will, and G. Winter, *Nucl. Phys.* **A226**, 157 (1974).
- [38] T. E. Ward and Y. Y. Chu, *Phys. Rev. C* **12**, 1632 (1975).
- [39] T. E. Ward, P. E. Haustein, J. B. Cumming, and Y. Y. Chu, *Phys. Rev. C* **10**, 1983 (1974).
- [40] T. E. Ward and P. E. Haustein, *Phys. Rev. C* **4**, 244 (1971).
- [41] H. J. Korner, F. E. Wagner, and B. D. Dunlap, *Phys. Rev. Lett.* **27**, 1593 (1971).
- [42] K. S. Krane, S. S. Rosenblum, and W. A. Steyert, *Phys. Rev. C* **14**, 656 (1976).
- [43] J. I. Zaitz and R. K. Sheline, *Phys. Rev. C* **6**, 506 (1972).
- [44] P. Christmas and P. Cross, *Nucl. Instrum. Methods* **174**, 571 (1980).
- [45] E. J. Konopinski, *The Theory of Beta Radioactivity* (Oxford University Press, London 1966).
- [46] L. V. Spencer, NBS Monograph 1 (U.S. Govt. Printing Office, September 10, 1959).
- [47] M. J. Berger, S. M. Seltzer, S. E. Chappell, J. C. Humphreys, and J. W. Motz, *Nucl. Instrum. Methods* **69**, 181 (1969).
- [48] L. J. Jardine and C. M. Lederer, *Nucl. Instrum. Methods* **120**, 515 (1974).
- [49] H. Bichsel, *Nucl. Instrum. Methods* **A235**, 174 (1985).
- [50] R.-D. Von Dincklage and J. Gerl, *Nucl. Instrum. Methods* **A235**, 198 (1985).
- [51] A. Carrington, H. W. Nicholson, and J. Krivicich, *Nucl. Instrum. Methods* **A248**, 425 (1986).
- [52] W. R. Nelson, H. Hirayama, and D. W. O. Rogers, The EGS4 Code System, Stanford Linear Accelerator Center Report No. SLAC-265, 1985 (unpublished).
- [53] D. W. O. Rogers, *Nucl. Instrum. Methods* **227**, 535 (1984).
- [54] H. Bichsel, private communication (1987).
- [55] R. Barden, Diplomarbeit, Mainz, 1985 (unpublished); *Verhandlungen Deutsche Physikalische Gesellschaften* **21**, 525 (1986).
- [56] E. B. Norman, S. E. Kellogg, T. Bertram, S. Gil, and P. Wong, *Appl. J.* **281**, 360 (1984).
- [57] C. B. Collins, C. D. Eberhard, J. W. Glesener, and J. A. Anderson, *Phys. Rev. C* **37**, 2267 (1988).
- [58] C. B. Collins *et al.*, *Phys. Rev. C* **42**, R1813 (1990).
- [59] Zs. Nemeth and F. Käppeler, Contribution to the International Symposium on Nuclear Astrophysics, Baden, Austria, 1990 (unpublished).
- [60] S. E. Kellogg and E. B. Norman (unpublished).
- [61] K. L. Hainebach, D. N. Schramm, and J. B. Blake, *Astrophys. J.* **205**, 920 (1976).
- [62] T. G. Harrison, *Astrophys. Lett.* **17**, 61 (1976).
- [63] T. G. Harrison, *Astrophys. Lett.* **18**, 8 (1976).
- [64] S. E. Woosley, D. H. Hartmann, R. D. Hoffman, and W. C. Haxton, *Astrophys. J.* **356**, 272 (1990).

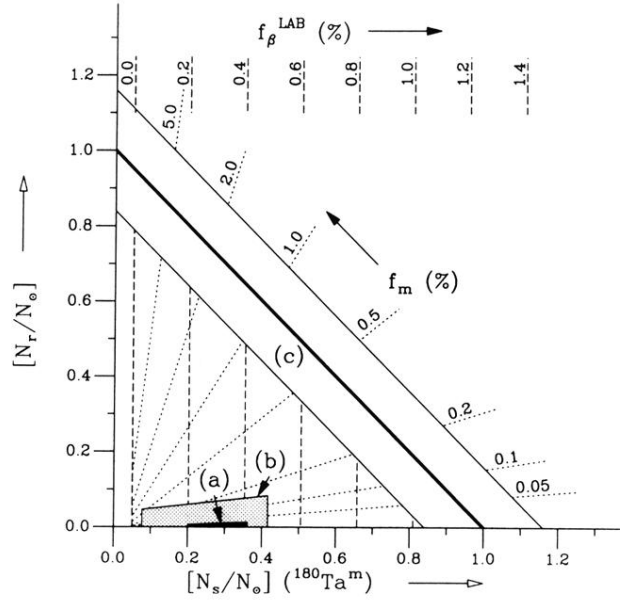


FIG. 13. Status of the Beer and Ward theory for the production of ^{180}Ta . Fractions of the observed solar-system abundance of $^{180}\text{Ta}^m$ produced in the s and r processes are used as the abscissa and ordinate of the plot. Superimposed are solutions to Eqs. (5) and (6) for laboratory-measured values of f_β and f_m assuming nominal s -process environmental conditions. Region (a) represents 68% confidence limits on our experimental measurements. Region (b) further includes the possible range of enhancement factors F_s^{enh} defined in Eq. (4) for other plausible stellar conditions in the neutron-capture processes. Region (c) represents uncertainties in the remaining input physics (abundances and neutron cross sections). Lack of an overlap between region (a) and the $N_s + N_r = N_\odot$ line, and even between the less-restrictive regions (b) and (c), force us to conclude that the Beer and Ward model cannot quantitatively account for all of the $^{180}\text{Ta}^m$ found in nature.